2000-11

Numerical Simulations of Steady and Pulsed Non-Adiabatic Magnetised Jets From Young Stars

Stephen O'Sullivan
Technological University Dublin, stephen.osullivan@tudublin.ie

Tom Ray
Dublin Institute for Advanced Studies

Recommended Citation

O'Suillivan, S. & Ray, T. (2000). Numerical simulations of steady and pulsed non-adiabatic magnetised jets from young stars. *Astronomy & Astrophysics* vol. 363, pg. 355-372. doi:10.21427/1bze-ag50

Astron. Astrophys. 363, 355–372 (2000)

ASTRONOMY AND ASTROPHYSICS

Numerical simulations of steady and pulsed non-adiabatic magnetised jets from young stars

S. O'Sullivan[1] **and T.P. Ray**[2]

[1] Department of Applied Mathematics, University of Leeds, Leeds LS2 9JT, UK
[2] Dublin Institute for Advanced Studies, 5 Merrion Square, Dublin 2, Ireland

Received 8 March 2000 / Accepted 26 April 2000

Abstract. In contrast to jets from radio galaxies, energy losses due to radiation effects, atomic hydrogen ionisation/recombination and molecular hydrogen dissociation are important in jets from young stars. Moreover there is now general agreement that magnetic fields may play a very important role not only in the formation of these jets but also their subsequent collimation.

With these ideas in mind we have developed a new multi-dimensional magneto-hydrodynamic second order upwind code that includes the above loss terms. Fluxes at cell interfaces are calculated using a linear approximation and, if this fails, a non-linear iterative solver. The condition $\nabla \cdot \mathbf{B} = 0$ is maintained by including small source terms in the conservation equations.

We find that the propagation dynamics and morphology of magnetised supersonic radiative jets are significantly different to their hydrodynamic counterparts even when β=$8\pi P_{gas}/B^2 \approx 1$. Both steady and pulsed jets were simulated. In particular, magnetic fields for the three configurations we tested (helical, toroidal, and poloidal) enhance the jet collimation. For example, longitudinal fields restrict the lateral motion of the flow and a purely toroidal field, through hoop stresses, constricts the jet towards its axis. Such stresses, in the toroidal field case, may lead to the jet exhibiting extended nose cones, enhanced bow shock speeds, and disruption of internal working surfaces (knots) formed by velocity variations in the jet. We find that poloidal fields maintain a more stable degree of collimation and knots are not destroyed. Cooling also improves the jet collimation as it reduces the thermal support in the cocoon making it narrower than its adiabatic counterpart. Another effect of cooling is that it gives rise to Rayleigh-Taylor (RT) unstable configurations at the head of the jet causing the bow shock to periodically break up into smaller structures that sank back into the jet cocoon. This could explain some of the knotty structures seen in Herbig-Haro bows.

Key words: Magnetohydrodynamics (MHD) – ISM: jets and outflows

Send offprint requests to: S. O'Sullivan (so@amsta.leeds.ac.uk)
Correspondence to: Department of Applied Mathematics, University of Leeds, Leeds LS2 9JT, England

1. Introduction

The simulation of astrophysical jets has a long history (e.g. Norman et al. 1982; Wilson & Scheuer 1983; Norman 1993). Most of the early work in the field concentrated on jets from radio galaxies. In part this was for historical reasons: jets from radio galaxies were the first to be discovered but in addition, because an essentially adiabatic equation of state could be assumed, they were easier to model than their nearer galactic counterparts i.e. Herbig-Haro (HH) jets from young stellar objects (YSOs). Many such examples of the latter are now known (see, for example, Ray 1996) since their discovery almost two decades ago. Their typical temperatures are around 10^4 K, so, in contrast to AGN jets, one has to allow for the effects of cooling by radiative recombination, ionisation and molecular dissociation.

Moreover, in the case of jets from radio galaxies, the importance of magnetic fields has been recognised for many years both from observational and theoretical perspectives (Laing 1993; Camenzind 1998). The concensus is that they are also important in the formation and subsequent collimation of YSO jets as well although observational evidence for their presence is much more difficult to come by (nevertheless see Ray et al. 1997 and Warren-Smith & Scarrott 1999).

One of the most striking features of the morphology of YSO jets, both from ground-based and Hubble Space Telescope images, is their knotty struture. Often these knots are quasi-periodically spaced, as in, for example, HH 34 or HH 111 (Ray et al. 1996; Reipurth et al. 1997). Although the precise origin of these knots is still debated (see, for example, Micono et al. 1998; Raga et al. 1998) there seems little doubt that at least some can be identified with internal working surfaces (Ray et al. 1996) caused by temporal variations in the outflow.

Simulations of YSO jets have now been performed (see, for example, Stone & Norman 1993; Stone & Norman 1994; Smith 1998) which include not only the energy loss terms but also the effects of "pulsing", i.e. velocity variations in the jet that in turn produce internal working surfaces (Raga et al. 1998). In this way many of the observed characteristics of YSO jets have been simulated. There are, however, some discrepancies: for example, the observed proper motions of the knots do not match

what one would expect on the basis that they are simple hydrodynamic internal working surfaces (Eislöffel & Mundt 1998).

Given the likely importance of magnetic fileds in the collimation jets, it is interesting to see what effects such fields have on their subsequent propagation. Moreover, since we are dealing with radiative jets in which large degrees of compression can occur, initially insignificant magnetic fields can become dynamically important through amplification. Thus even if such fields are not important for collimation purposes, this does not mean they can be subsequently ignored. It is also not clear what effects magnetic fields have on the development of internal working surfaces. With these ideas in mind, we have simulated a number of YSO jet configurations using a new magneto-hydrodynamic second order upwind code that includes energy losses due to radiation effects, atomic hydrogen ionisation/recombination and molecular hydrogen dissociation. The $\nabla \cdot \mathbf{B}$=0 condition is preserved to tuncation error accuracy by including small source terms in the conservation equations.

Outline details of the code are given in Sect. 2 before we present and discuss our results for the three magnetic field configurations used (helical, toroidal, and poloidal). We examine both steady and "pulsed" jets. It is shown that even quite modest magnetic fields, through amplification by compression, can have dramatic effects on jet development when compared with the corresponding hydrodynamic cases. This is especially true for the evolution of internal working surfaces in pulsed jets.

2. Code

The usual equations of ideal magnetohydrodynamics govern the dynamics of the jets

$$\frac{\partial \rho}{\partial t} + \nabla \cdot (\rho \mathbf{u}) = 0 \tag{1}$$

$$\frac{\partial (\rho \mathbf{u})}{\partial t} + \nabla \cdot (\rho \mathbf{u}\mathbf{u} + \mathbf{I}p^* - \mathbf{B}\mathbf{B}) = 0 \tag{2}$$

$$\frac{\partial \mathbf{B}}{\partial t} + \nabla \cdot (\mathbf{u}\mathbf{B} - \mathbf{B}\mathbf{u}) = 0 \tag{3}$$

$$\frac{\partial E}{\partial t} + \nabla \cdot ((E + p^*)\mathbf{u} - (\mathbf{u} \cdot \mathbf{B})\mathbf{B}) + \mathcal{L} = 0 \tag{4}$$

$$p^* = p + \frac{1}{2}B^2 \tag{5}$$

$$E = \frac{1}{2}\rho u^2 + \frac{p}{\gamma - 1} + \frac{1}{2}B^2 \tag{6}$$

where $\mathbf{I}$ is the identity dyadic and $\mathcal{L}$ is the energy loss due to radiation, dissociation and ionisation, and the other symbols have their usual meanings. Here units are chosen such that $\mathbf{B}$ has absorbed a factor of $1/(\sqrt{4\pi})$. These equations are derived from the classical equations of hydrodynamics and Maxwell's equations of electrodynamics under the assumptions that charge separation and displacement current may be neglected. Flux freezing and non-relativistic flow speeds are also assumed.

The absence of magnetic monopoles is demanded via

$$\nabla \cdot \mathbf{B} = 0 \tag{7}$$

If this constraint is ever true then it is true for all time for a system governed by these equations by virtue of Eq. (3). However, truncation errors introduced by finite differencing the equations mean that, from a numerical perspective, Eq. (7) must be handled by the explicit inclusion of terms proportional to $\nabla \cdot \mathbf{B}$ in the MHD equations (Powell 1994). These terms may be derived from the primitive equations of electrodynamics by relaxing Eq. (7).

A new second order accurate MHD code was developed for cooled astrophysical flows governed by Eqs. (1)–(4) and Eq. (7). This code is a hybrid of various techniques and for a complete desciption the reader is referred to O'Sullivan (2000). Fluxes at cell interfaces are calculated by means of a linear Riemann solver, or, if the solution is not physical, a robust non-linear Riemann solver. The non-linear solver uses the jump conditions for shocks and integrates across rarefactions with magnetosonic switch-off waves and the degenerate waves resulting from a vanishing longitudinal magnetic field treated separately as special cases. Pressure positivity is maintained when integration of the ideal MHD equations results in a negative pressure by resorting to one of three alternatives. In order of sophistication and application the options are: an entropy density advection technique based on a simplified set of equations valid when no shocks are present in the local flow (Balsara & Spicer 1999); reverting to a first order solution to take advantage of its inherent numerical diffusivity; and lastly, injecting thermal energy to retrieve positive pressure.

In order to include the effects of radiative energy loss, ionisation, and dissociation represented by $\mathcal{L}$ in Eq. (4) we separate these processes by operator splitting the dynamical timestepping from the cooling. Thus, after each step in time, the chemistry is calculated in the resultant state over the same period. We do not consider structure in the cell when applying the chemistry routines to the second order state because it would be extremely time-consuming to do so and we find that the morphology of the kind of flows considered here are rather insensitive to the cooling. Therefore the cooling in these simulations is not second order in space, but is second order accurate in time. The ionisation fraction of H and dissociation fraction of H_2 are explicitly calculated and cooling from atomic species is found using rates for a plasma of solar abundances (Sutherland & Dopita 1993). The dissociation rates are obtained from cross sections derived by Martin & Keogh (1998) for collision-induced dissociation from the $H_2(0,0)$ ground vibration-rotation state with partners H, H_2, H_e, and e^-. The molecular cooling function used is from Lepp & Schull (1983); calculated using four vibrational levels, each with 21 rotational states. The reader is referred to Appendix A for further details.

3. Initial conditions and presentation of results

We consider the propagation of jets in molecular environments under a range of conditions. In all cases we use an initial ambi-

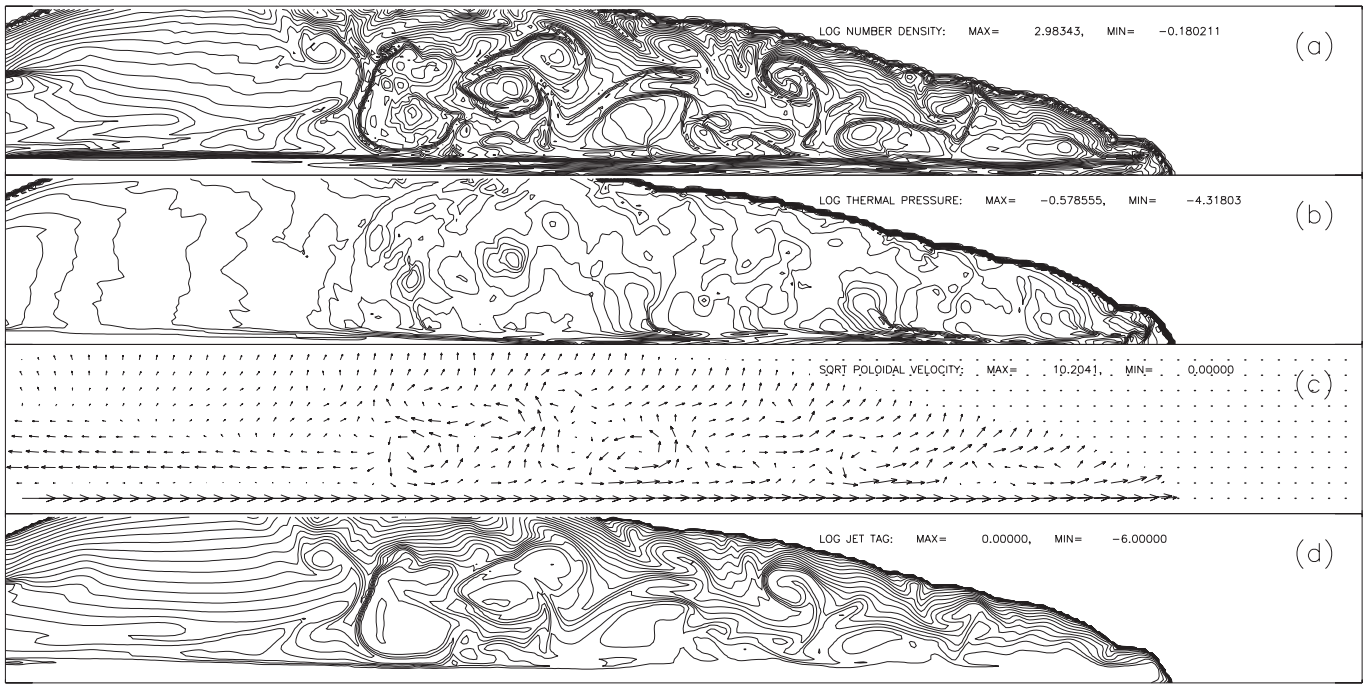

Fig. 1a–d. Adiabatic molecular jet with no magnetic field present at $t = 1000$ yr. All results are displayed for this time unless otherwise stated. The scale of the grid is 2.0×10^{17} cm by 2.5×10^{16} cm.

ent medium of uniform thermal pressure and density. We choose a temperature of $T = 10^2$ K and a nuclear number density of $n = 50\,\mathrm{cm}^{-3}$ as being characteristic of the outer regions in molecular clouds and assume a ratio of atomic to molecular hydrogen of 1 ($\eta_{\mathrm{H}} \equiv n_{\mathrm{H}_2}/n_{\mathrm{H}} = 1$, where n_{H_2} and n_{H} are the number densities of atomic and molecular hydrogen respectively). For the jet conditions we also use $n = 50\,\mathrm{cm}^{-3}$ and look at molecular jets with $\eta_{\mathrm{H}} = 1$ at a temperature $T = 10^3$ K, and atomic jets at $T = 10^4$ K. We do not consider cooling processes below $T = 10^3$ K so the molecular jets are initially in thermal equilibrium. The atomic jets, however, undergo cooling immediately upon entering the grid. Low densities are used in order to better resolve the cooling length scales which go as the inverse of the density squared. Clearly both of these cases are over-pressurised with respect to the surrounding material, the latter very much so, and therefore strong constraining processes will need to take effect in order to prevent the jet losing its collimation to rapid expansion once it enters the ambient material.

Cylindrical coordinates under axial symmetry (z, r, ϕ) (longitudinal, radial, and azimuthal coordinates respectively where ϕ is the ignorable coordinate) are used on a the grid with dimensions 2.0×10^{17} cm by 2.5×10^{16} cm with a cell of length 1.0×10^{14} cm in each coordinate direction. The inflow velocity of the jet is chosen to be close to $100\,\mathrm{km\,s}^{-1}$. We use a jet Mach number of $M_a \equiv u_0/a_j = 40$ for the molecular jets and $M_a = 10$ for the atomic jets, where a_j is the sound speed in the jet and u_0 is the inflow velocity (all Mach numbers refer to wave-speeds within the jet beam unless otherwise indicated). This gives values for u_0 of $104\,\mathrm{km\,s}^{-1}$ and $103\,\mathrm{km\,s}^{-1}$ respectively. A 10% sinusoidal variation is imposed on u_0 for the pulsed molecular jet simulations. The inflow aperture radius, R_j, is 25 cells with an additional 5 cells for a smeared interface between the jet and the ambient material. In the smeared layer the velocities, number densities, and thermal pressure are all given a hyperbolic tangential profile between their jet and ambient values to dampen the effect of excessive shear viscous heating due to too sharp a discontinuity. All simulations are run for 1000 years, except those for which an earlier time was chosen to prevent the head of the jet from propagating off the grid. A Courant number of 0.6 is used.

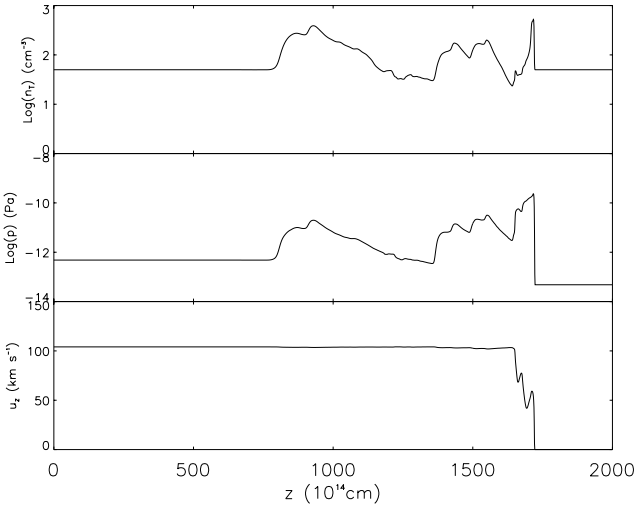

Fig. 2. Length-ways section of jet beam at 20% of the jet radius for an adiabatic molecular jet with no magnetic field present.

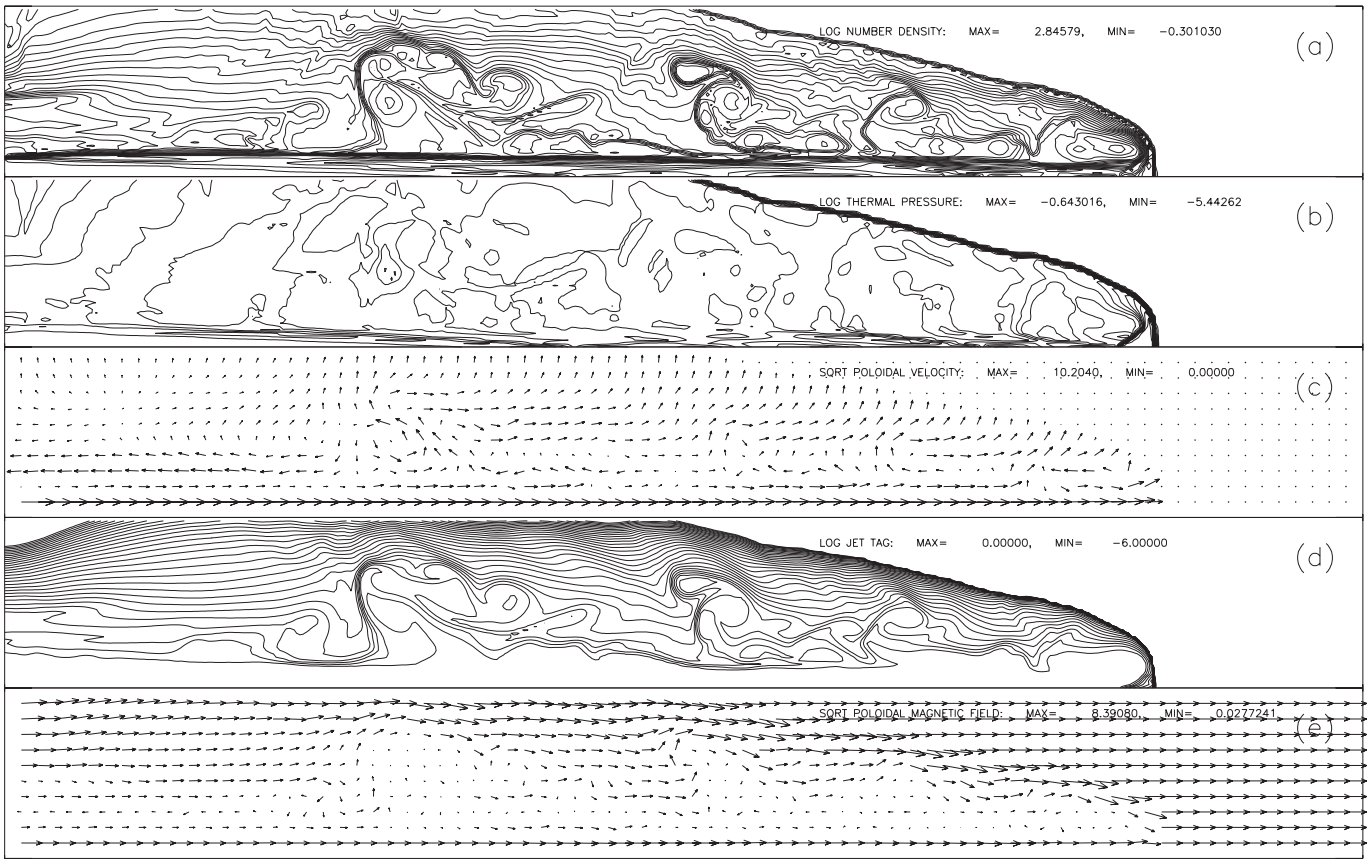

Fig. 3a–e. Adiabatic molecular jet with a longitudinal magnetic field.

Material is permitted to freely enter and leave the grid at the downwind and upper boundaries by assigning zero-gradient boundary conditions there. The boundary cells at the inflow aperture are set independently of the grid cells. At the upwind boundary outside the inflow aperture we use inflow boundary conditions rather than reflecting since according to the analysis of Kössl & Müller (1988) reflecting boundary conditions are probably more appropriate for jet simulations close to the driving source and outflow boundary conditions for simulations of jets far from the source. At the $r = 0$ symmetry axis reflecting boundary conditions are used.

We examine the role of magnetic fields under different configurations in the propagation and morphology of the jets. Four different initial configurations are considered, each in a simple form justifiable in the context of YSO jets: baseline zero field, uniform longitudinal field permeating both the jet and ambient material, purely toroidal field within the jet beam only, and a force-free helical field. All fields are chosen to be approximately in equipartition with the jet (ie. $\beta \equiv p_m/p_{th} = 1$ where p_m and p_{th} are the magnetic and thermal pressures respectively). Clearly, this requires a much stronger field in the case of the higher temperature atomic jet than in the molecular case (about 4 times greater).

3.1. Poloidal magnetic field

The configuration we consider here, a straightforward longitudinal field permeating both the jet and ambient material with the form $\mathbf{B} = (B_0, 0, 0)$, is supported by observations which suggest that jets from YSOs have a preferential alignment with their main direction of propagation along the local interstellar magnetic field (Strom & Strom 1987). Requiring initial equipartition of the magnetic and thermal pressures within the beam of the jet gives a field strength $B_0 = 11\mu$G and $B_0 = 42\,\mu$G for the molecular and atomic jets respectively. From this we get Alfvén Mach numbers $M_A = 35$ and $M_A = 9$ for the molecular and atomic jets where $M_A \equiv u_0/c_A$ and c_A is the usual Alfvén speeds given by $c_A^2 = B_0^2/\rho$. The magnetosonic Mach speeds M_B are then given by $M_B^{-2} = M_a^{-2} + M_A^{-2}$ (26 and 7 respectively).

3.2. Toroidal magnetic field

Having considered the most simple of purely poloidal field configurations it makes sense to examine the effects of a purely toroidal field which, by symmetry, can only have a radial dependence, $\mathbf{B} = (0, 0, B(r))$. In our simulations of this case we use the same form as Lind et al. 1989 (hereafter LPMB). Following LPMB, the field adopted corresponds to a uniform

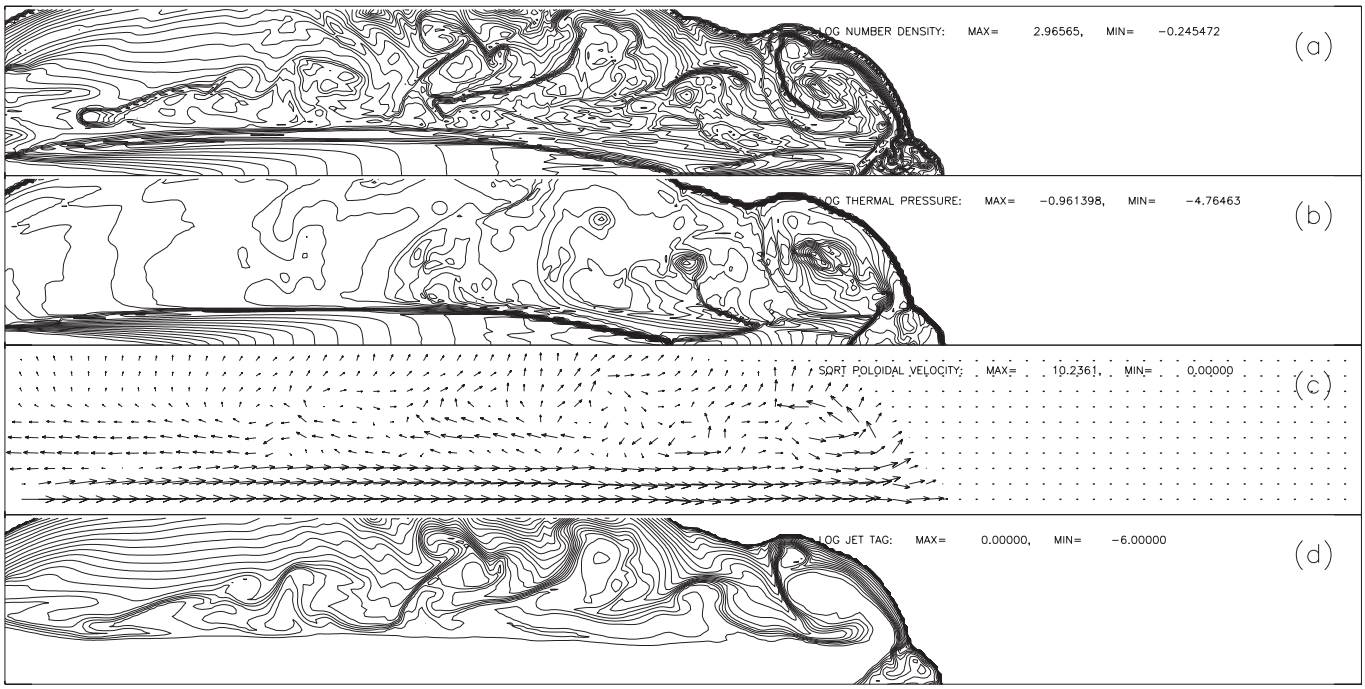

Fig. 4a–d. Adiabatic atomic jet with no magnetic field present.

current density within a core radius R_m of the jet and a return current sheath at the jet boundary R_j

$$B(r) = \begin{cases} B_m \frac{r}{R_m} & 0 \le r < R_m \\ B_m \frac{R_m}{r} & R_m \le r < R_j \\ 0 & R_j \le r \end{cases} \quad (8)$$

Imposing initial hydromagnetic equilibrium on the jet we have

$$\nabla \cdot (\mathbf{I}p^* - \mathbf{BB}) = 0 \quad (9)$$

which, in axisymmetry, becomes

$$\frac{dp}{dr} + \frac{B}{r}\frac{d(rB)}{dr} = 0 \quad (10)$$

Integrating by parts we get

$$p(r) = p(0) - \frac{1}{2}B^2 - \int_0^r \frac{B^2(r')}{r'}dr' \quad (11)$$

where the integral term on the right hand side is due to the hoop stress.

Defining the pressure at $r = R_j$ to be p_{edge} gives

$$p(0) = p_{edge} + \int_0^{R_j} \frac{B^2(r')}{r'}dr' \quad (12)$$

Using the definition of LPMB

$$\overline{\beta} \equiv \frac{R_j^2 p_{edge}}{\int_0^{R_j} B^2(r')r'dr'} \quad (13)$$

is the ratio of the mean internal gas pressure to the mean internal magnetic pressure. From Eqs. (13) and (8) we can solve for R_m to obtain

$$R_m = R_j \exp\left(0.25 - \frac{1}{2\overline{\beta}(1-\alpha)}\right) \quad (14)$$

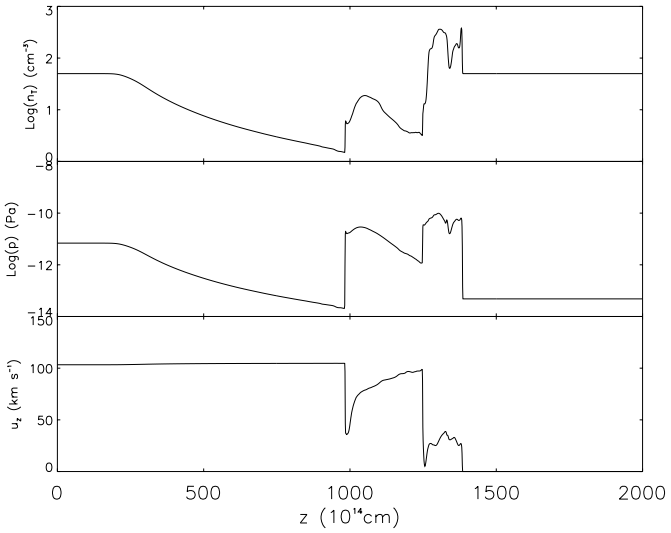

Fig. 5. Length-ways section of jet beam at 20% of the jet radius for an adiabatic atomic jet with no magnetic field present.

where

$$\alpha = 1 - \frac{1}{\beta_m}\left(\frac{R_m}{R_j}\right)^2 \quad (15)$$

and

$$\beta_m \equiv \frac{p_{edge}}{\frac{1}{2}B_m^2} \quad (16)$$

By means of the equation for the thermal pressure under hydromagnetic equilibrium, Eq. (11), we have from Eq. (8)

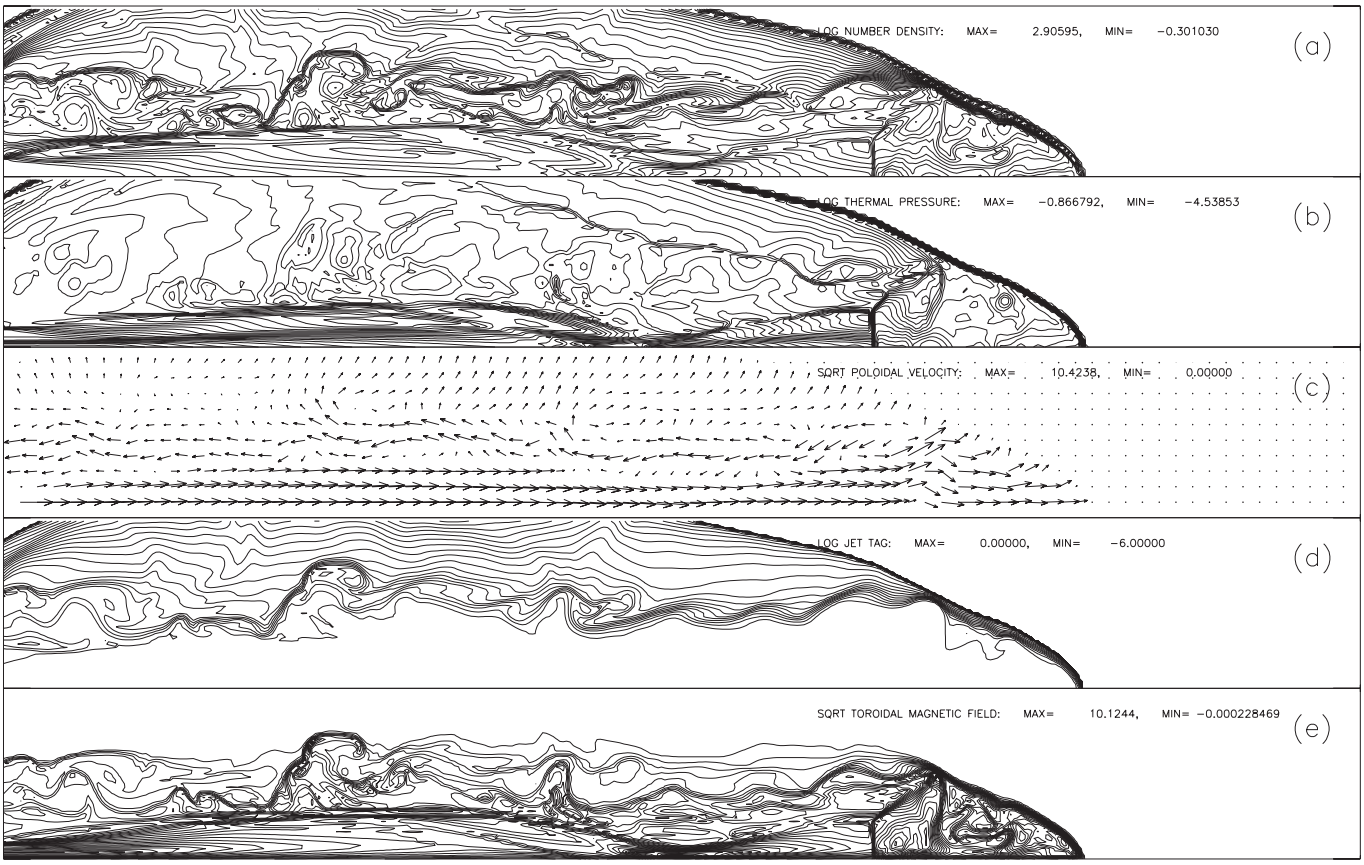

Fig. 6a–e. Adiabatic atomic jet with a toroidal magnetic field.

$$p(r) = \begin{cases} \left(\alpha + \frac{2}{\beta_m}\left(1 - \frac{r^2}{R_m^2}\right)\right) p_{edge} & 0 \le r < R_m \\ \alpha p_{edge} & R_m \le r < R_j \\ p_{edge} & R_j \le r \end{cases} \quad (17)$$

The model we have used is given by a choice of parameters $(\alpha, \overline{\beta}) = (0.5, 1)$. This corresponds to the values $B_m = 16\,\mu$G and $B_m = 62\,\mu$G for the molecular and atomic jets respectively, $R_j = 2.5 \times 10^{15}$ cm, and $R_m = 1.2 \times 10^{15}$ cm. The average Mach numbers are calculated by integrating the wave-speeds across the jet beam and are given by

$$\overline{M} \equiv \frac{R_j u_0}{\sqrt{2\int_0^{R_j} c^2 r' dr'}} \quad (18)$$

where c is the wave-speed pertinent to the Mach number being calculated. We get $\overline{M}_A = 35$, and $\overline{M}_B = 27$ for the molecular jet, and $\overline{M}_A = 9$, and $\overline{M}_B = 7$ for the atomic jet.

3.3. Helical magnetic field

The other adopted configuration is a force-free helical field taken from Todo et al. 1993:

$$B_z(r) = B_0 \sqrt{1 - \frac{Ar^2(r+d)}{\left(r + \frac{1}{2}d\right)^3}} \quad (19)$$

$$B_r = 0 \quad (20)$$

$$B_z(r) = B_0 \sqrt{\frac{Ar^2 d}{2\left(r + \frac{1}{2}d\right)^3}} \quad (21)$$

where, following Todo et al. 1993, we set the arbitrary constants A and d to 0.99 and three times the jet radius respectively. B_0 is the value of the magnetic field strength on the axis which we choose to be the initial equipartition value on the axis. Thus, $B_0 = 11\,\mu$G and $B_0 = 42\,\mu$G for the molecular and atomic jets respectively. From this we get $M_A = 37$, and $M_B = 27$ for the molecular jet, and $M_A = 10$, and $M_B = 7$ for the atomic jet.

This field configuration is force-free and, being helical, should show characteristics of both the purely poloidal and purely toroidal fields described above. The pitch angle of this field at the jet radius is approximately 0.33 radians.

3.4. Presentation of results

The results for the simulations are presented in three formats. We make use of square root scaled vector field plots for the poloidal velocity and magnetic fields with the data set rebinned to 80×10 points. Additionally, in order to more clearly represent the flow outside the beam, the vectors' magnitudes are normalised so that the maximum length is twice the spacing between the sample points. Contour plots with 30 levels between the maximum and minimum values over a data set rebinned to 400×50 points as a smoothing measure, are plotted (when rel-

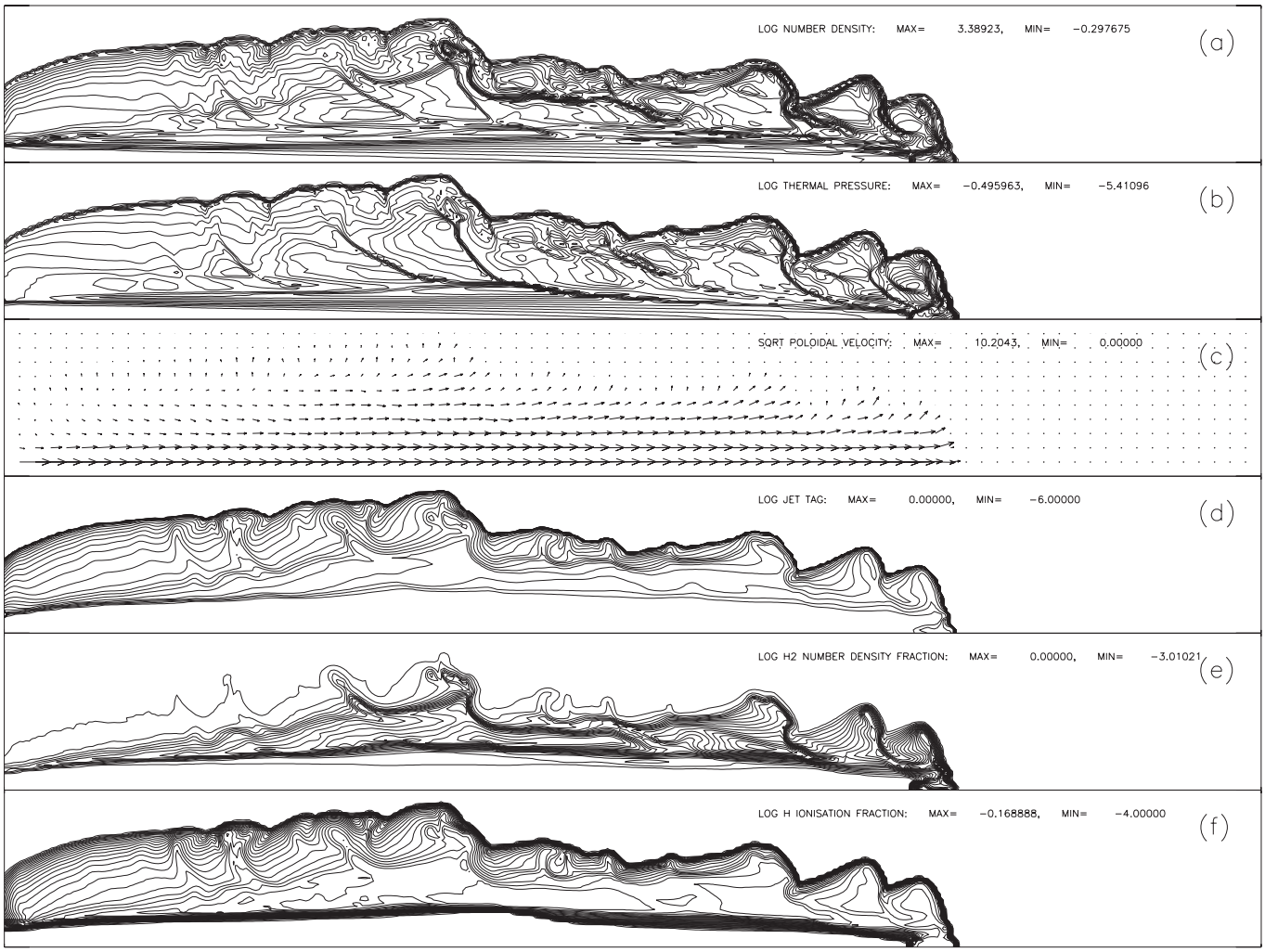

Fig. 7a–f. Radiative molecular jet with no magnetic field present.

evant) for the total nuclear number density, thermal pressure, jet material fraction, H_2 number density, H ionisation fraction, toroidal velocity, and toroidal magnetic field component. A log scale is used for all quantities except the toroidal components of the velocity and magnetic fields when a square root scale is used. The maximum and minimum values are inset on the plots. Finally, axial sections of the jets at 20% of the jet radius, referred to as R_s, are presented. We choose a non-zero radius at which to take this section because an on-axis section is prone to non-physical features such as the carbuncle effect (Quirk 1992), and a *slating* effect related to the vanishing radial coordinate in which material gathers on the axis to produce excessively high densities (Blondin et al. 1990). We should point out that, for these reasons, the solutions provided close to the axis should be interpreted with care as the evolution of the jet on-axis may have been affected. The density and pressure are given to log scale and the remainder to linear. For reasons of conciseness only sufficient plots are presented in this paper to support the main points made in the accompanying text.

4. Steady adiabatic magnetised jets

4.1. Molecular

The usual bow shock/jet shock configuration is evident in Figs. 1 and 3. The flow is prevented from becoming stationary by the interaction between the internal crossing shocks and the vortices in the cocoon. These crossing shocks are amplified by Kelvin-Helmholtz instability effects and thus the propagation of the jet is essentially time-dependent (Kössl & Müller 1988). The vortices within the cocoon are prompted by the interaction of the crossing shocks within the beam and the working surface at the head of the jet and hence have a similar separation to the spacing of these shocks. For each of the jets, the pressure within the head is large enough to confine the beam near the head and further upstream the crossing shocks work towards maintaining a collimated beam. Fig. 2 illustrates the effects of two crossing shocks and the bow shock on the state within the jet. The beam is maintained at a uniform pressure and density until the first crossing shock has propagated from the edge of the jet to R_s. This occurs at about 82×10^{15} cm as would be

expected from a sonic Mach number of 40. Beyond this point the incidence of crossing shocks is not so easily predicted due to the impingement of disturbances from vortices shed from the head as it ejects material into the cocoon.

Fig. 3 shows an adiabatic molecular jet with a longitudinal magnetic field at t = 1000 yrs. The striking differences between it and the jet illustrated in Fig. 1 are in the shape of the head of the jet and the higher propagation velocities of the bow shock. The simulations in which the initial magnetic field carries a longitudinal component have flattened nose cones and have had their propagation retarded by about 6×10^{15} cm^3 with respect to the hydrodynamic and toroidal field cases. The jets are initially over-pressurised and thus undergo an expansion and crossing shocks propagating from the edge of the beam inwards produce higher densities on axes. This focusing gives a narrower, more ballistic form to the nose cone, however, in the cases where there is a longitudinal field component the lateral motion of the beam is constrained and the nose cone is blunt. The magnetic field does not play a more significant part in the development of the cocoon because the dynamics are dominated by the high pressure gradients.

4.2. Atomic

As one might expect, for very over-pressurised jets (the thermal pressure ratio for these simulations is about 100) there is a strong initial tendency for the beams to expand upon entering the low pressure ambient material. The hydrodynamic case illustrated in Fig. 4 shows an initial strong expansion and subsequent re-collimation by oblique internal shocks within the beam. The nose is far blunter than in the molecular case due to the greater support provided by the higher pressure of the post shock material. The vortices established are large and disperse the jet material into the cocoon very efficiently reducing the ballistic nature of the nose cone and hence lessening the propagation distance by 32×10^{15} cm. We can see better the action of the almost immediate expansion, due to the high sound speeds, in the section plots of Fig. 5. The expansion is only halted as the crossing shock, which re-collimates the beam at later times, reaches R_s. The forward and reverse shocks are also clearly visible in both the pressure and density plots. It is noteworthy that the axial velocity is briefly reduced to less than 40 km s^{-1} by the crossing shock after which it recovers before being attenuated again by the reverse shock at the head.

However, as we have chosen $\beta = 1$ the magnetic fields are sufficient to provide the same constraint to the lateral motions of beam material as in the molecular case. The Alfvén Mach numbers are roughly 4 times lower than for the molecular conditions and hence the structures within the jet are more dramatically affected. The purely poloidal case is tightly constrained by the magnetic field and the cocoon is tightly wrapped about the beam. The nose is blunt as in the molecular case and the vorticity is damped within the cocoon. Kelvin-Helmholtz instabilities are evident in the material within the cocoon. The toroidal field case in Fig. 6 shows the nose cone typical of such simulations (eg. Clarke et al. 1986, LPMB). There is a large

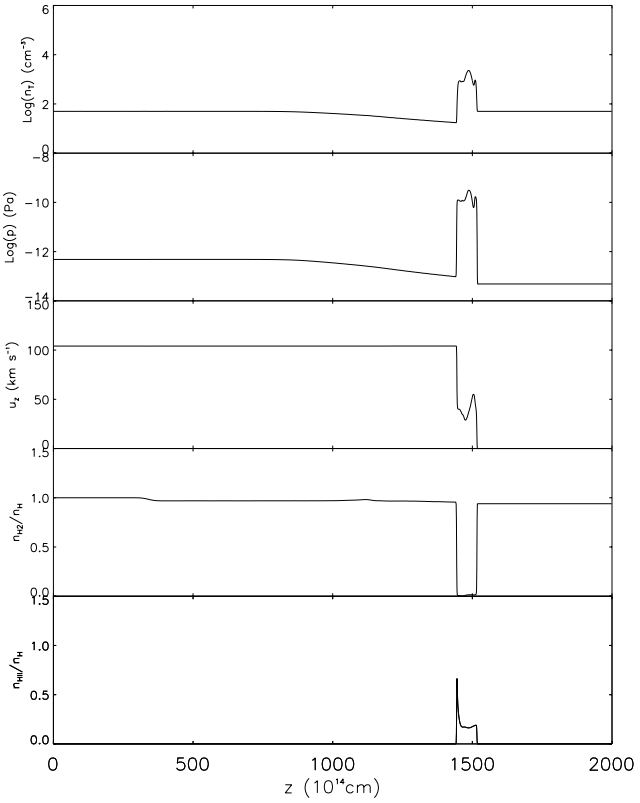

Fig. 8. Length-ways section of jet beam at 20% of the jet radius for a radiative molecular jet with no magnetic field present.

separation between the reverse shock and the forward shock on the nose cone. The reverse shock consists of an axisymmetric triple point formed by the intersection of a strong planar shock over the central part of the beam and two oblique shocks extending away from it. This extended nose cone structure is formed by the pinching effect of the magnetic hoop stresses. Material which would otherwise be ejected sideways into the cocoon is held between the forward and reverse shocks and high pressures are created which accelerate the bow shock forward. It has been pointed out by Frank et al. 1998 that the speed at which the nose cone propagates through the ambient material is attributable to the hoop stresses induced by the magnetic field bringing about a more streamlined profile to the bow rather than simply to magnetic pressures as previously believed (see Kössl et al. 1990a, Kössl et al. 1990b). The helical field case shows features characteristic of both the longitudinal and toroidal field configurations; the nose cone being slightly extended and the beam constrained although there is more vorticity in the cocoon due to stronger crossing shocks within the beam of the jet.

5. Steady cooled magnetised jets

5.1. Molecular

The hydrodynamic cooled molecular jet shown in Fig. 7 shows an entirely different morphology to the adiabatic jet shown in Fig. 1. As has been remarked in previous work (e.g.,

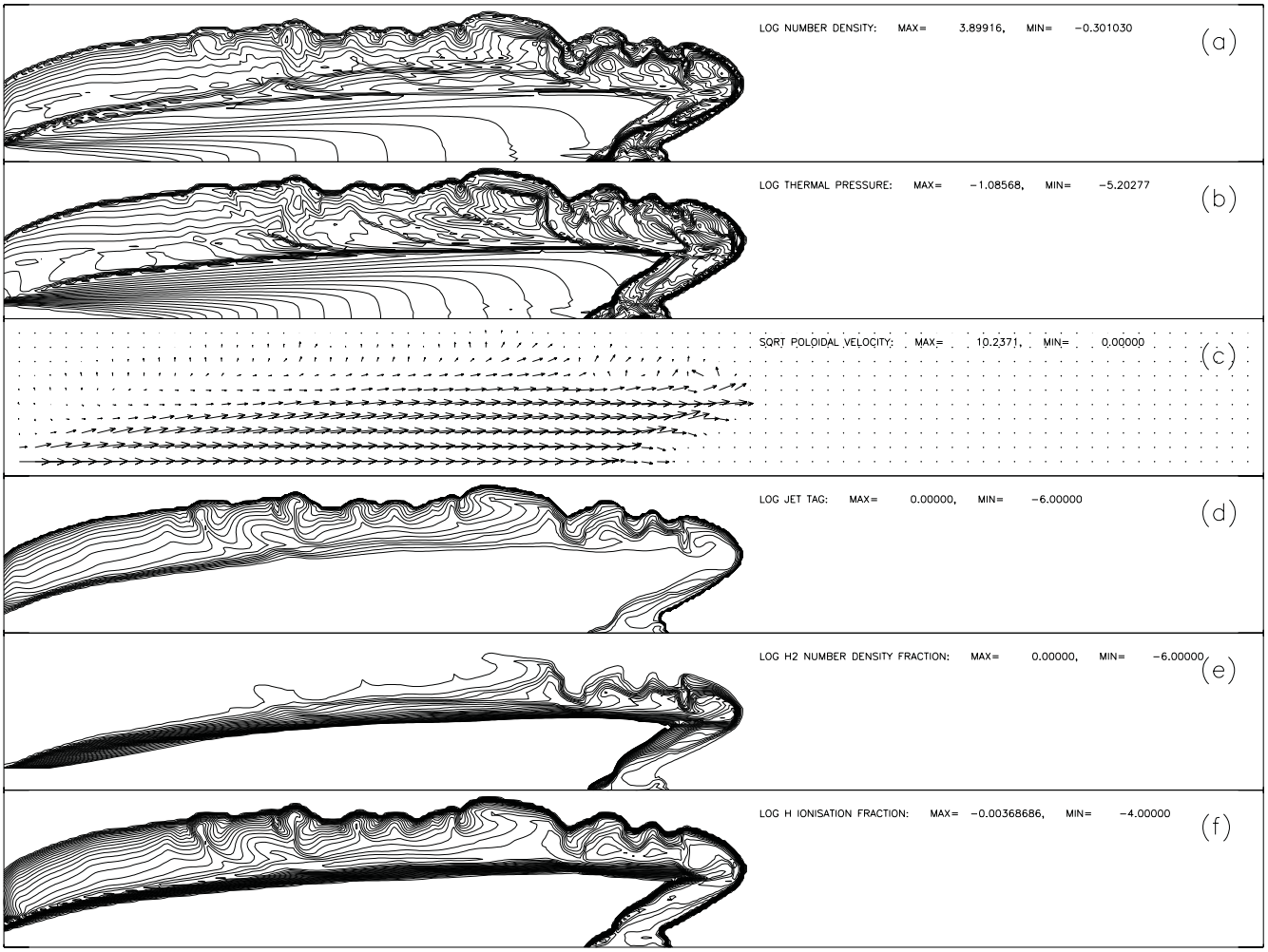

Fig. 9a–f. Radiative atomic jet with no magnetic field.

Blondin et al. 1990, Stone & Norman 1994) the head of the jet is dynamically unstable and disrupts into clumps. The disruption is a combined effect of non-uniform cooling and the RT instability. Oblique shocks are driven into the beam of the jet near the head by the high pressure of the surrounding material in the cocoon. As a result of the increased post-shock densities the cooling lengths are diminished and a dense annulus is formed through which the more tenuous, cooling gas is forced by the high post-shock pressure. This gas is accelerated into the jet head as the annulus begins to narrow by the de Laval nozzle mehanism and it pushes on the thin shell of cool, dense material at the leading edge of the head. The resultant acceleration into the less dense ambient material causes the shell to become RT unstable and it fragments. The period of the instabilities near the head of the jet is about 60 years which is comparable with the RT growth time $t_{RT} \approx 20\,\mathrm{yr}$ in the shell where we have used

$$\frac{t_{RT}}{t_j} \approx \frac{2u_0}{100\,\mathrm{km\,s^{-1}}} \tag{22}$$

from Blondin et al. 1990. Here $t_j \equiv R_j/u_0$ is the dynamical timescale of the jet.

It should also be noted that there are no strong crossing shocks in the beam of the jet. We can see clear evidence of this in Fig. 8 where the profiles of the state variables are relatively featureless in comparison with the adiabatic counterparts. This means that the jet is not as effective at forcing its path through the ambient material due to a less focused nose cone. It can be seen from the density and pressure plots in Fig. 8 that the stagnation region between the forward and reverse shocks at the head is almost isothermal. The compression ratios are higher than those in the adiabatic case because of the loss of pressure support in this region due to collisionally induced radiative cooling. There is also complete dissociation of H_2 in this zone as well as a high H ionisation fraction, particularly at the reverse shock where there is a pronounced spike. The number densities of the molecular hydrogen and the ionisation fraction are important quantities as these can be related to observations. The weaker bow shock wings and the oblique shocks (which have low post-shock temperatures) at the reverse jet shock only partly dissociate the H_2 allowing the regions behind the bow shock wings to have relatively high molecular abundances. Further back along the bow shock there are greater number densities of H_2 due to the weaker

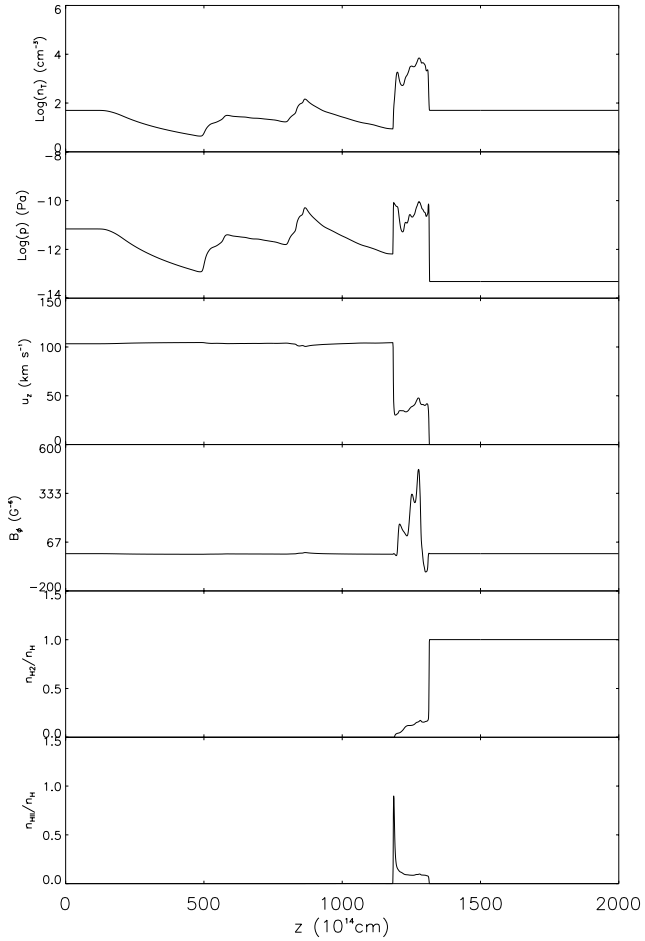

Fig. 10. Lengthways section of jet beam at 20% of the jet radius for a radiative atomic jet with a helical magnetic field.

and more oblique bow shock wings. From the plots of the jet tag (which indicates the jet material fraction) it is clear that most of the H_2 within the post-bow shock region has come from the jet. Since we have not allowed H_2 reformation, as the time-scales are very long in typical cocoon environments, this material must have passed through the jet shock and survived long enough to re-expand into the wake. The jet shock and bow shock are too weak to achieve a complete ionisation of the atomic hydrogen with a typical cocoon ionisation fraction of $\frac{1}{2}$.

Although not shown here (see O'Sullivan (1999)), the RT instability is damped by the presence of a longitudinal field which supports the bow shock against collapse, but is still evident with a purely toroidal field. It should be noted that Cerqueira et al. 1997 observed significant fragmentation of the head for an axial field. This discrepancy might be attributable to the differences in initial conditions, in particular their higher densities and hence shorter cooling lengths. For the toroidal field the jet has been accelerated through the action of hoop stresses focusing the beam so that it punches a hole through the ambient material in an almost ballistic manner. The nose cone is about 55×10^{15} cm more advanced than for the longitudinal field case. The jet head has propagated about 25×10^{15} cm further than the adiabatic toroidal case, demonstrating that the effect of cooling amplifies the acceleration effect due to the pressure support of the dense plug of material in the nose cone being radiated away and allowing it to be further compressed. It should be noted that to some degree the sharpness of the nose cone's profile is exaggerated by the cylindrical geometry as the radial coordinate approaches zero. The helical field case (for the parameters we have chosen) is more reminiscent of the longitudinal than the toroidal field simulations. It shows the irregular bow shock characteristic of a cooled jet but with damping by the longitudinal field component. The extent of damping, however, is less than the corresponding purely longitudinal case.

5.2. Atomic

An interesting difference between the adiabatic unmagnetised jet in Fig. 4 and the cooled unmagnetised jet in Fig. 9 is the unchecked expansion of the latter. To some degree this is counter-intuitive as we have seen that if material can be focused to a narrow region the cooling will prevent the high pressures generated from re-expanding the material in this region. The essential point here is that there is very little preventing the over-pressurised beam from expanding as the cooling damps the reflection shocks which re-collimate the beam in the adiabatic case. A consequence of this is that the bow shock has a concave profile which allows large parts of the molecular material passing through it to survive.

The longitudinal field provides a sufficiently strong field to prevent the expansion of the beam seen in the unmagnetised case. The overall features are very similar to the adiabatic counterpart but with the cocoon more tightly wrapped about the beam and the ejecta forming very strong vortices. The purely toroidal field case shows a cocoon with a less turbulent flow within and a more expanded beam. The reasons for this are similar to those described for the unmagnetised jet. The crossing shocks are very clear in the beam. The helical field case in Figs. 10 and 11 shows characteristics of the other simulations. The beam is constrained from expanding by the longitudinal component and has a sharply focused nose cone due to the toroidal field. The strong vortices seen in the longitudinal case are also present. Fig. 10 illustrates the action of the crossing shocks within the jet beam. The stagnation region is clear in all variables. The sharp spike in the H ionisation fraction is again visible at the reverse shock. Note the rapid dissociation of molecular hydrogen on passing through the bow shock.

6. Pulsed cooled magnetised jets

In this section we consider the effects of variability in the jet inlet velocity for cooled jets. This is of interest due to observational evidence for the presence of knotty emission structures in the main beam of YSO jets. Although pulsing of jets has been studied in some depth (Suttner et al. 1997; Biro & Raga 1994; Gouveia Dal Pino & Benz 1994; Stone & Norman 1993), a full treatment under the influence of cooling and magnetic fields has not been published before now. We wish to examine the effects

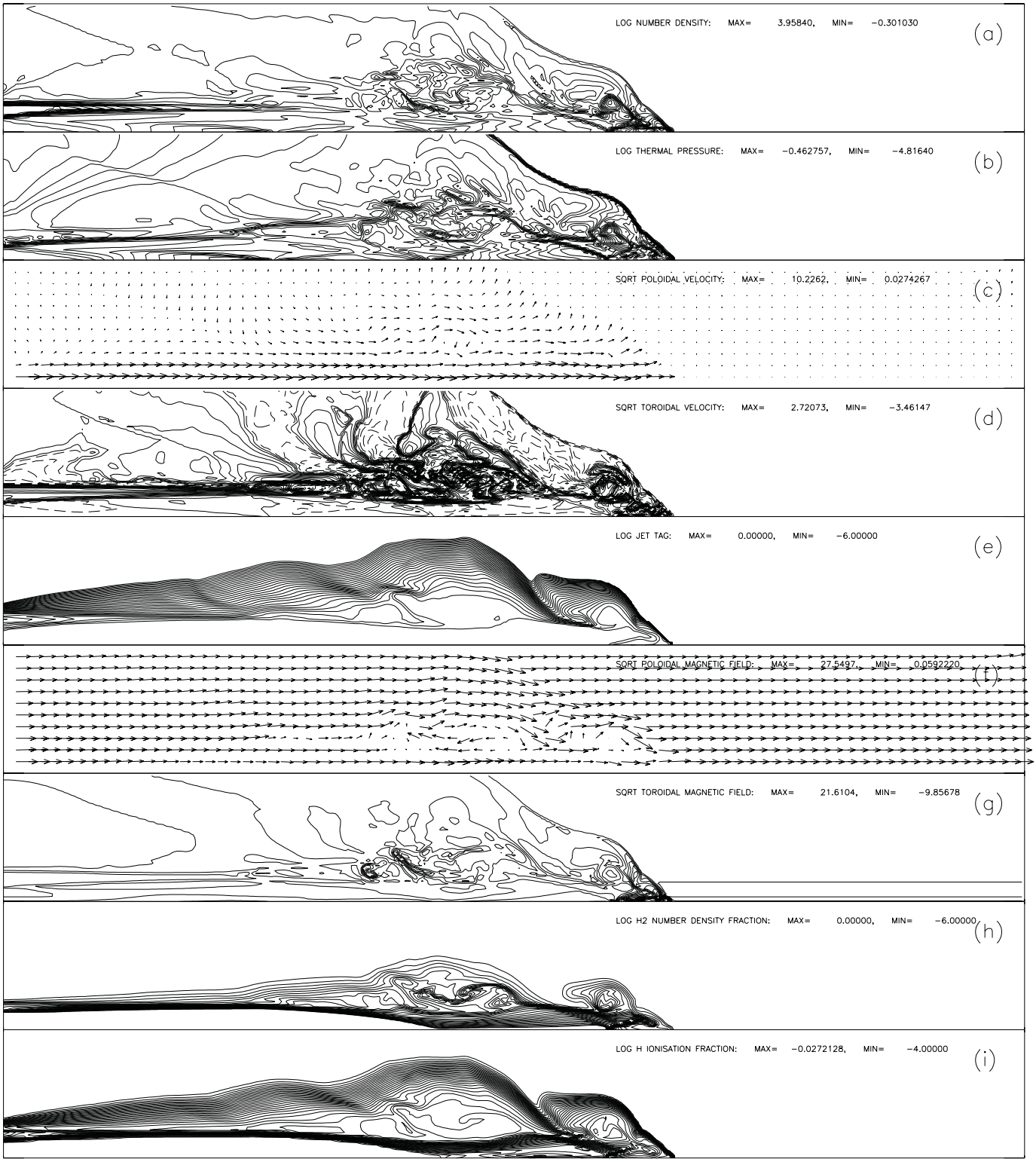

Fig. 11a–i. Radiative atomic jet with a helical magnetic field.

of fields on the structure and development of these knots in cooled jets. We consider the range of initial field configurations examined in the previous sections only for the molecular jets with an inflow velocity given by

$$u(t) = u_0 \left(1 + \frac{1}{10}\sin(\omega t)\right) \tag{23}$$

where $\omega = 2\pi/100\,\mathrm{year}^{-1}$. Thus the magnitude of the velocity variation at the source is about $20\,\mathrm{km\,s}^{-1}$.

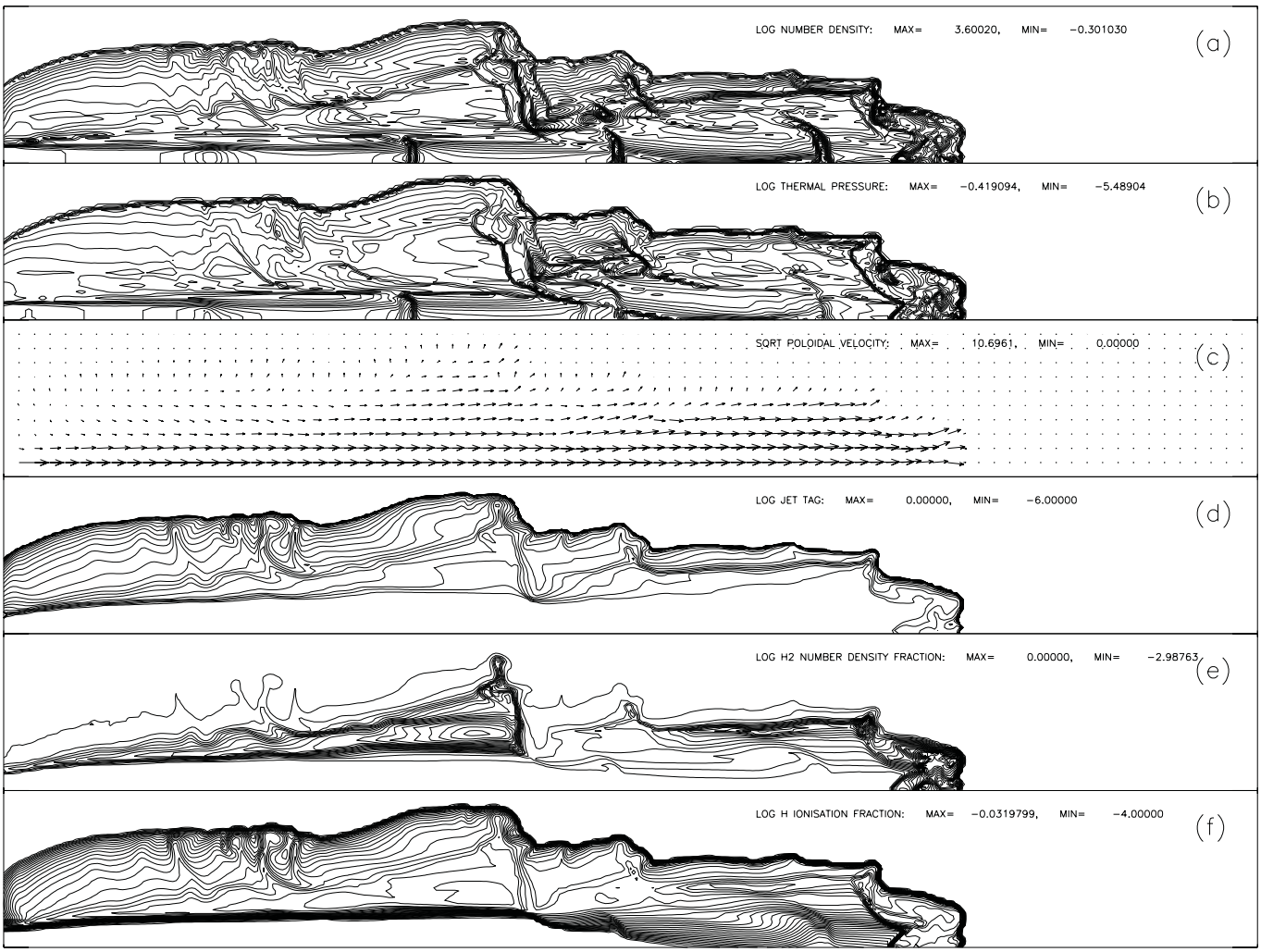

Fig. 12a–f. Pulsed, radiative molecular jet with no magnetic field.

6.1. Molecular

Fig. 12 shows the results of a simulation for an adiabatic unmagnetised molecular jet with a pulsed inflow velocity after 1000 years. It can be seen that the pulsing has dramatically affected the shape of the bow shock. The pulses take some time to steepen into shocks. As we move from the left the most recent pulse has not yet steepened into a shock structure. The subsequent pulses show the evolution of the pulses with time as they move towards the head of the jet. Initially, they steepen into a two shock structure known as an internal working surfaces (IWS). This consists of an upstream shock moving more slowly than the jet velocity which decelerates the material being driven into it, and a downstream shock moving more quickly than the material in front of it and sweeping up the material in front of it. It can be seen that the IWS is initially very narrow but that it widens and broadens as it squeezes more and more material sideways into the cocoon until it reaches the head of the jet where it is disrupted. Upon being broken up, it leaves shock structures in the wake of the jet which are visible in the cocoon. When IWS interacts with a crossing shock, as can be seen in Fig. 12, the high post shock temperatures result in an increase in the ionisation of the atomic hydrogen and in the dissociation of H_2.

For the magnetised jet simulations the results again show the pulses steepening into forward and reverse shock structures but their development is significantly altered by the presence of the magnetic fields. For the longitudinal field case the widening of the knots in the direction transverse to jet axis is hindered by the field and the knots remain close to the same width. The toroidal field influence on the knots is even more dramatic. It should be pointed out that the jet in this case has become very focused due to the influx of the high density IWSs into the head and has travelled the full extent of the grid in 900 years. The jet is plotted in Fig. 13 at this time as opposed to the 1000 years used in all other cases. The hoop stresses eventually break the IWSs up as they are squeezed radially. There is strong compression of the toroidal field within the IWSs and their interaction with the crossing shocks causes some ionisation and dissociation of the atomic and molecular hydrogen respectively towards the nose. For the helical case illustrated in Fig. 14 it can be seen that

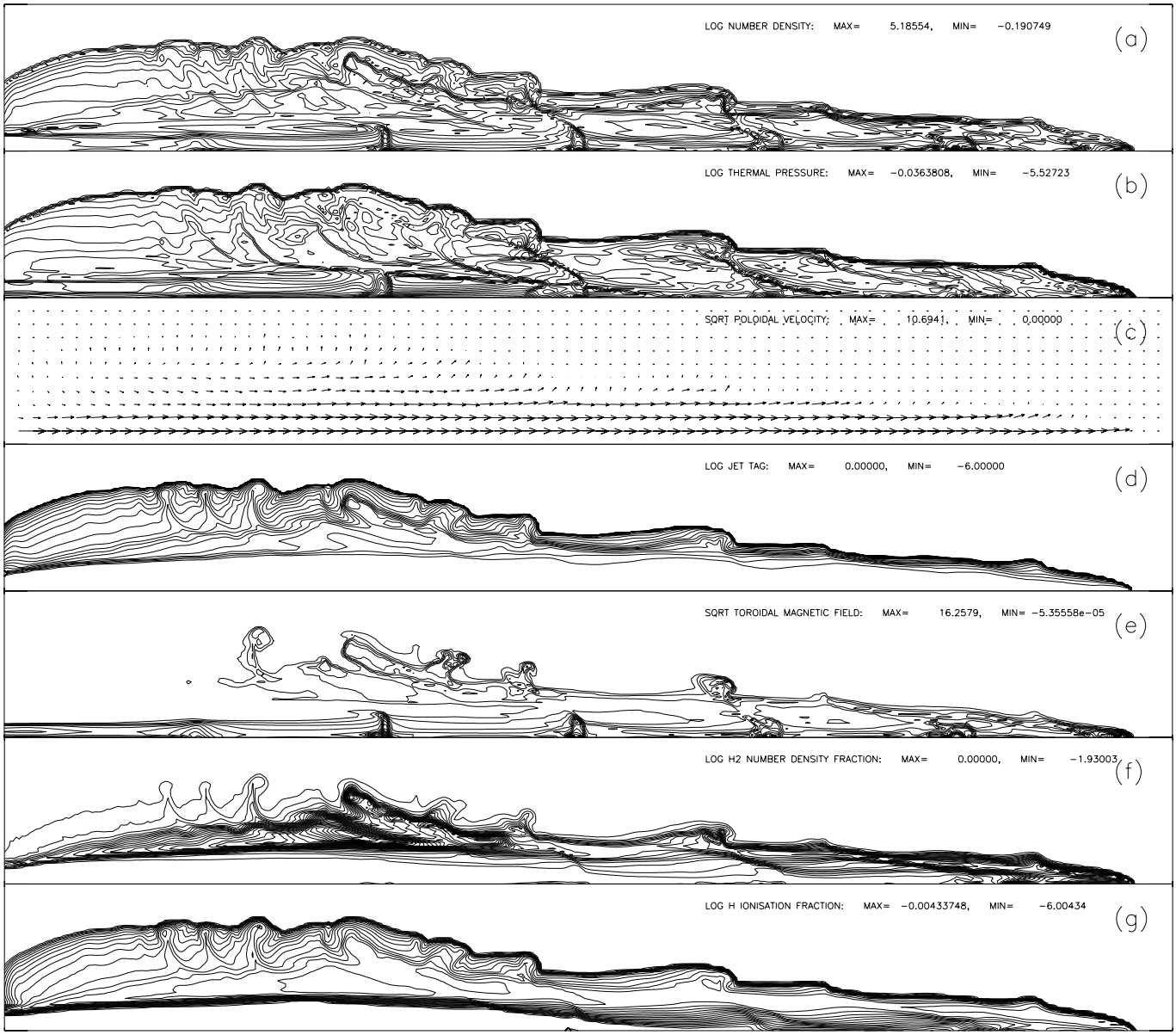

Fig. 13a–g. Pulsed, radiative molecular jet with a toroidal magnetic field. The jet has reached the edge of the grid here after only 900 yrs.

the pulsing has resulted in the formation of a pronounced nose cone structure which has advanced about 25×10^{15} cm further than the non-pulsed case. The IWSs can be seen to broaden and develop extended, swept back wings which feed material from the jet into the cocoon. The axial section plots given in Fig. 15 show that the pulses take up to 200 years to steepen into shocks. The amplitude of the velocity jump across the shocks is quite large at about 20 km s^{-1} (7.7 times the sound speed). A signature of the pulse driven shocks is the narrow compression spikes in the toroidal magnetic field component. Beyond the point where the first crossing shock is incident noise has begun to disrupt the profiles of the pulse driven shocks in velocity, pressure, and density. It is interesting to note however, that these spikes in B_ϕ endure intact.

7. Conclusions

The effects of cooling, magnetic fields, and sinusoidal variation of the inflow velocity have been examined for over-pressurised atomic and molecular jets with parameters chosen to be appropriate to YSO flows. Three magnetic field configurations, as well as an unmagnetised baseline case, were used: a purely poloidal longitudinal field of constant magnitude permeating both the jet and ambient material; a purely toroidal field within a current carrying jet; and a force-free helical field permeating both the jet and ambient material.

In agreement with previous results, it was found that the presence of cooling reduces the pressure support in post-shock regions and hence the bow shock is narrower than for the adiabatic cases. It was also observed that the head of the jet is subject

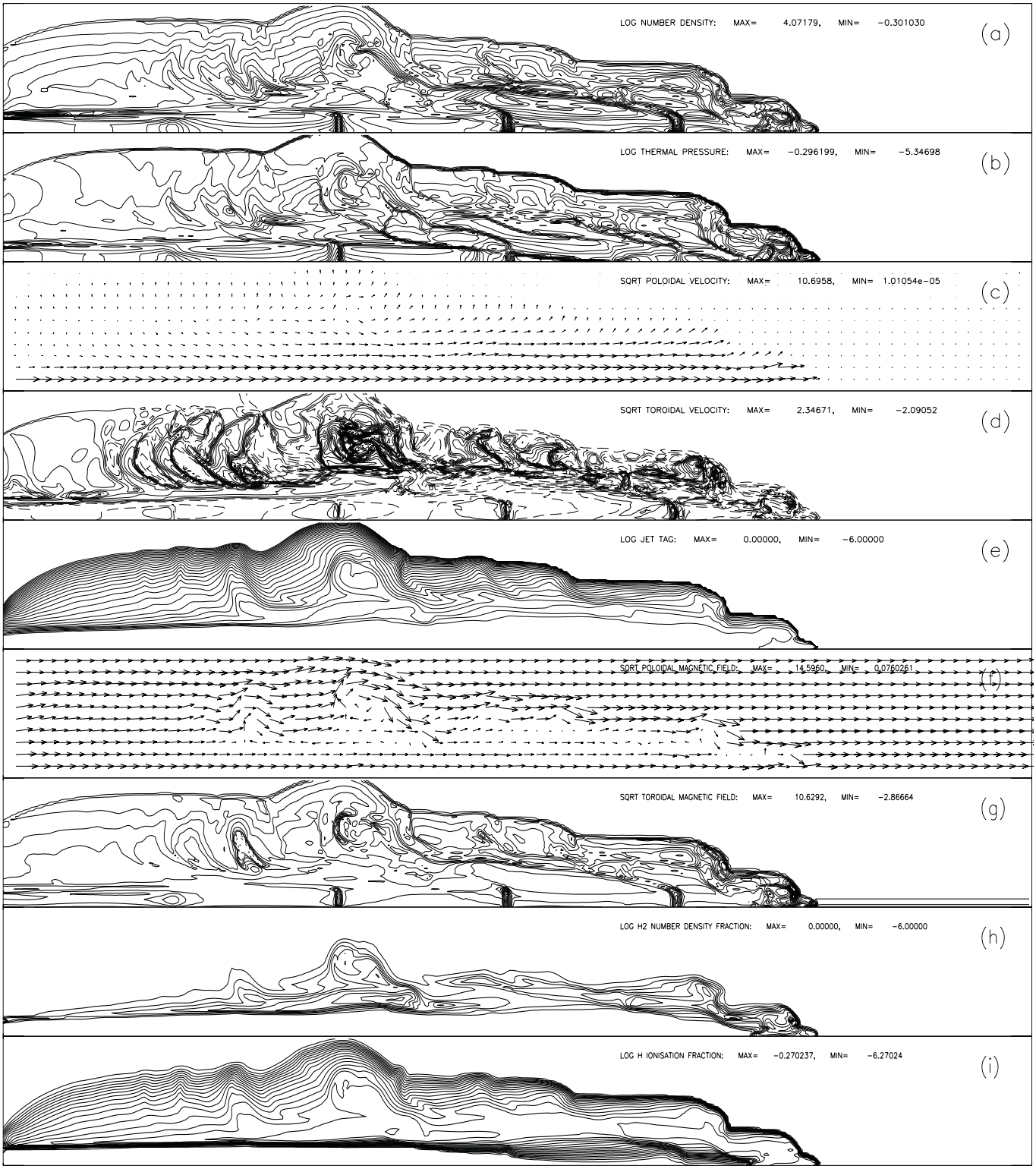

Fig. 14a–i. Pulsed, radiative molecular jet with a helical magnetic field.

to disruption due to the combined effects of non-uniform cooling and the RT instability which causes it to fragment producing an irregular profile for the bow shock unlike the parabolic shape seen for the adiabatic jets. Another effect of the cooling is that the reflection shocks caused by the jet expanding laterally into the ambient medium are damped and therefore are unable to recollimate the jet as efficiently as in the adiabatic case. As a result the very over-pressurised unmagnetised atomic jet expands rel-

atively unchecked upon entering the grid. It was noted that there is usually complete dissociation of molecular hydrogen in the stagnation zone and significant atomic hydrogen ionisation. In almost all cases the ionisation fraction is greater at the jet shock side of the working surface for the parameter space we have studied.

The introduction of physically justifiable equipartition magnetic fields was shown to have pronounced effect on the propagation dynamics and morphology of the jets. In all cases the head of the jet had an altered shape and as a result there were differences in the propagation velocities. As with previous studies, it was observed that a toroidal field will exert hoop stresses on the jet beam thereby restricting the lateral flow of over-pressurised material in the stagnation zone between the forward-facing bow shock and the backward-facing jet shock. This results in an extended nose-cone and an accelerated bow shock. It was noted that a longitudinal field component similarly helps to maintain a focused beam and damps the RT fragmentation of the bow shock. However, in this case the field lines prevent lateral motion in either direction and so the nose presents a much flatter profile to the ambient medium. Similar results to these have recently been found by Stone & Hardee (2000).

Simulations of molecular jets with a sinusoidally varying inflow velocity were performed to see what effects this might have on the jet. Variability may be a sufficient explanation for the knots seen in a large number of HH flows: it was found that for the unmagnetised case the pulses gradually steepen into IWSs consisting of an upstream shock that decelerates material moving into it, and a downstream shock sweeping up the material in front of it. It was shown that the IWS begins life as a very narrow structure but widens and broadens as more material enters it and is squeezed out to the sides into the cocoon. Once the IWS reaches the termination shock of the jet it is disrupted and leaves subsidiary shock structures in the body of the cocoon. It was also found that when an IWS interacts with a crossing shock there is increased H ionisation and H_2 dissociation. The first results of pulsed cooled magnetised jets were then presented. These showed that, as for the hydrodynamic case, the pulses in the inflow velocity steepened into IWSs but that their dynamical evolution and morphology was significantly altered by the presence of magnetic fields. For the longitudinal field the spreading of the knots into the cocoon is damped because the post-shock material is impeded from leaving the working surface. This results in broader knots within the main beam of the jet. The effect of the toroidal field on the development of the knots was found to be even more dramatic: with thermal support being lost to radiative cooling, the hoop stresses crush the knots completely. It was also shown that, for the helical field when there is a poloidal field component to support the knots, the compression spikes of the toroidal field component were robust signatures of the knots.

Acknowledgements. We would like to thank Sam Falle, Dan Spicer, Turlough Downes and Luke Drury for their assistance with the development of the code and John Walsh for maintaining the Beowulf cluster at the Dublin Institute for Advanced Studies. Thanks are also due to the referee, Jim Stone, for his helpful comments.

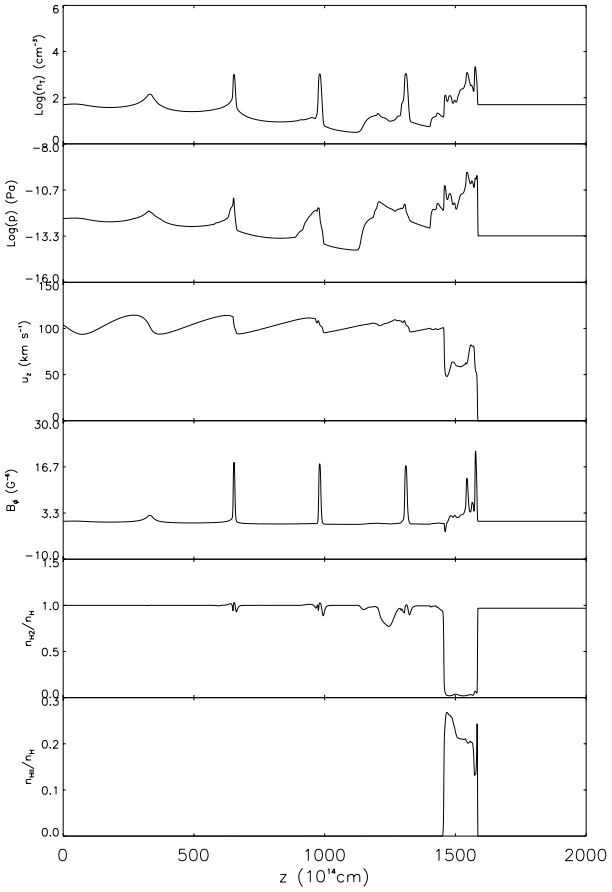

Fig. 15. Lengthways section of jet beam at 20% of the jet radius for a pulsed, radiative molecular jet with a helical magnetic field.

Appendix A: cooling

A.1. Atomic radiative cooling

The radiative energy losses due to atomic processes are calculated using a function obtained from Sutherland & Dopita (1993). Their model structure is that of a cooling slab of plasma, initially in collisional ionisation equilibrium, which is followed during its approximately isobaric cooling flow. For our simulations we have chosen to use a function based on a model in which a plasma of solar abundances (see Table A.1) is cooling from $\log(T)$=6.5 down to $\log(T)$=4.0. Collisional ionisation equilibrium is not assumed and the diffuse radiation field is taken to be zero (essentially assuming that the plasma is optically thin). The net cooling function of the plasma considers collisional line radiation, free-free and two-photon continuum, recombination processes, photo-ionisation heating, collisional ionisation, and Compton heating:

$$\Lambda_{net}(T) = \Lambda_{lines} + \Lambda_{cont} \pm \Lambda_{rec} - \Lambda_{photo} + \Lambda_{coll} \pm \Lambda_{Compton} \quad \text{(A.1)}$$

The cooling function is stored as a table of $\log(\Lambda_N)$ versus $\log(T)$ where

$$\Lambda_N(T) = \frac{\Lambda_{net}}{n_t n_{\rm e}} \quad \text{(A.2)}$$

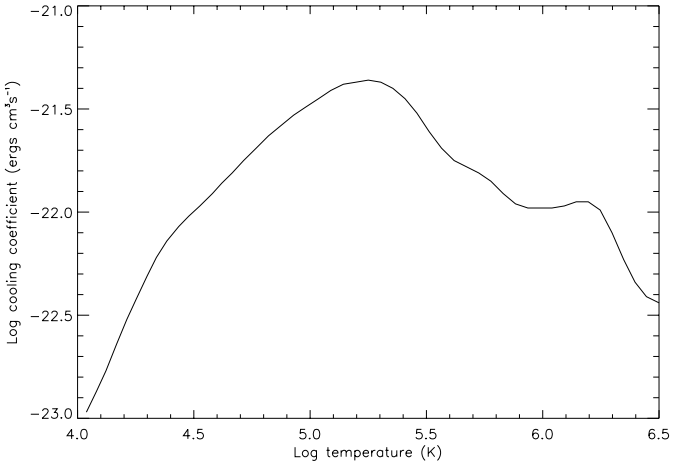

Fig. A.1. Plot of log normalised cooling rate (ergs cm^3 s^{-1}) against log temperature (K).

and n_t and $n_{\rm e}$ are the ion and electron number densities respectively. Linear interpolation is used to determine values between entries on the table. The cooling function is plotted in Fig. A.1.

A.2. Atomic hydrogen ionisation and recombination

We wish to calculate the ionisation fraction of atomic hydrogen explicitly. It may be inferred from the atomic cooling model described above but this would be inappropriate because the initial ionisation fraction will, in general, not lie on the cooling curve of the model. We therefore maintain a fixed ionisation fraction during the atomic cooling substep and correct the energy deficit in the total energy once the ionisation has been explicitly calculated. It is easy to show (see Falle & Raga 1995) that

$$\frac{\partial e_r}{\partial t} + \nabla \cdot ((e_r + p)\mathbf{u}) = -\mathcal{L} - \beta_H I_r \tag{A.3}$$

where e_r is the reduced energy equal to the thermal plus the kinetic energy, $\beta_{\rm H}$ is the ionisation potential of hydrogen ($= 1.002 \times 10^{13}$ erg g^{-1}), and I_r is the ionisation rate for hydrogen. I_r is found using the rates given by Falle & Raga 1995.

$$I_r = n_{\rm e}(n_{\rm H} - n_{\rm e})C(T) - n_{\rm e}^2 R(T) \tag{A.4}$$

where $n_{\rm e}$ is the electron number density, $n_{\rm H}$ is the non-molecular hydrogen number density, and

$$C(T) = K_C T^{0.5} \exp\left(\frac{-1.579\times10^5 K}{T}\right) \tag{A.5}$$

$$R(T) = K_R T^{-0.7} \tag{A.6}$$

where $K_C = 6.417\times10^{-11}$ cm^3 s^{-1} K$^{-0.5}$, and $K_R = 2.871\times10^{-10}$ cm^3 s^{-1} K$^{0.7}$ are the collisional ionisation and radiative recombination rates respectively.

A.3. Molecular hydrogen cooling

The molecular cooling function used is from Lepp & Schull (1983). It was calculated using four vibrational levels, each with 21 rotational states. The level populations were determined by balancing downward radiative and collisional rates with collisional excitation, neglecting rates to and from higher levels. Only $\Delta J = 0, \pm 2$ transitions were considered. The resultant radiative cooling rate $\Lambda_{\rm H_2}$ is fitted to a sum of terms representing vibrational and rotational cooling from both H-H_2 and H_2-H_2 collisions,

$$\Lambda_{\rm H_2} = n_{\rm H_2}\left[\frac{L_{vH}}{1+\frac{L_{vH}}{L_{vL}}} + \frac{L_{rH}}{1+\frac{L_{rH}}{L_{rL}}}\right] \tag{A.7}$$

where the vibrational cooling coefficients at high and low temperature are

$$L_{vH} = (1.10\times10^{-13}\text{ergs s}^{-1})\exp\left(-\tfrac{6744K}{T}\right) \tag{A.8}$$

$$\begin{aligned} L_{vL} \;=\; & [n_{\rm H}k_{\rm H}(0,1) + n_{\rm H_2}k_{\rm H_2}(0,1)] \\ & \times(8.18\times10^{-13}\text{ergs}) \end{aligned} \tag{A.9}$$

where the terms $k_{\rm H}(0,1)$ and $k_{\rm H_2}(0,1)$ are the $v = 0 \rightarrow 1$ collisional excitation rates for transitions involving H and H_2 respectively. Since cooling due to H_2-H_2 interactions are only important for low temperatures (Lepp & Schull 1983), we ignore the $k_{\rm H_2}(0,1)$ contribution. $k_{\rm H}(0,1)$ is defined as

$$k_{\rm H}(0,1) = \begin{cases} (1.0\times10^{-12})T^{\frac{1}{2}}\exp\left(-\frac{1000\,\rm K}{T}\right) & \text{if } T > 1635\,\rm K \\ (1.4\times10^{-13})\exp\left[\frac{T}{125\,\rm K} - \left(\frac{T}{577\,\rm K}\right)^2\right] & \text{otherwise.} \end{cases} \tag{A.10}$$

The rotational cooling rate coefficients at high and low density are

$$L_{rH} = \begin{cases} (3.90\times10^{-19}\text{ergs s}^{-1})\exp\left(-\frac{6118\,\rm K}{T}\right) & \text{if } T > 1087\,\rm K \\ \text{dex}(-19.24 + 0.474x - 1.247x^2) & \text{otherwise} \end{cases} \tag{A.11}$$

Table A.1. Solar abundances (from Anders & Grevesse 1989)

	$\log(n/n_{\rm H})$		$\log(n/n_{\rm H})$
H	0.00	C	-3.44
O	-3.07	Na	-5.67
Al	-5.53	S	-4.79
Ar	-5.44	Fe	-4.33
He	-1.01	N	-3.95
Ne	-3.91	Mg	-4.42
Si	-4.45	Cl	-6.50
Ca	-5.64	Ni	-5.75

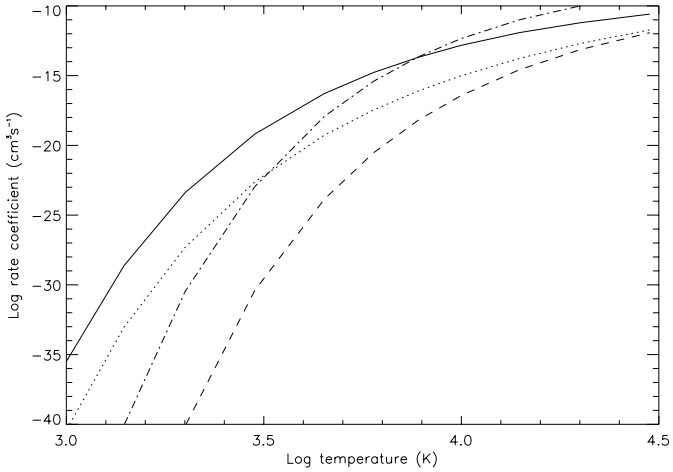

Fig. A.2. Log rate coefficients (cm^3 s^{-1}) for dissociation of $H_2(0,0)$ for four different collision partners plotted against log temperature (K). *Solid curve*: H, *dotted curve*: H_2, *dash-dotted curve*: e, and *dashed curve*: H_e.

and

$$\frac{L_{rL}}{Q(n_{H_2}, n_H)} = \begin{cases} (1.38 \times 10^{-22}\text{ergs s}^{-1})\exp\left(-\frac{9243\,\text{K}}{T}\right) \\ \qquad\qquad \text{if } T > 4031\,\text{K} \\ \text{dex}(-22.90 - 0.553x - 1.148x^2) \\ \qquad\qquad \text{otherwise} \end{cases} \tag{A.12}$$

where $x = \log(\text{T}/10^4\text{K}$ and

$$Q(n_{H_2}, n_H) = n_{H_2}^{0.77} + 1.2 n_H^{0.77} \tag{A.13}$$

is a function which bridges the gap between the low density ($\Lambda_{H_2} \propto n^2$) and high density ($\Lambda_{H_2} \propto n$) limits of the cooling. This function is valid between 100 K and 1.0×10^5 K. We can justify setting the molecular cooling to zero above this range because the number densities of H_2 will be very low at these high temperatures due to collisional dissociation. It is worth noting that we have included the effects of vibrational energy level transitions here but have not in the energy equation. The cooling due to the vibrational levels only becomes significant around 7×10^3 K and at this temperature the dominant energy loss due to H_2 is dissociation.

A.4. Collision induced dissociation of molecular hydrogen

The dissociation rates are obtained from cross sections derived by Martin & Keogh (1998) for collision-induced dissociation from the $H_2(0,0)$ ground vibration-rotation state with partners H, H_2, H_e, and e^-. These coefficients are plotted in Fig. A.2.

A.5. Non-uniformity of γ

Obviously differential dissociation of molecular hydrogen gives rise to a non-isotropic γ. This means that for the Riemann problem described Sect. 2 there may be a different γ on each side of the interface. We handle this complication by assuming that no dissociation occurs across the waves for the time being. Thus, it is the contact discontinuity which carries the jump in γ and consequently we use the left state value for regions to the left of the contact and vice-versa.

A.6. Inclusion of cooling effects in numerical scheme

In dealing with a radiatively cooled jet we must consider a number of time-scales. These are the the cooling time, the ionisation time, and the dissociation time. For the type of densities that are used in this work, the ionisation time-scale is extremely short and in strong shocks we do not resolve it. This may result in an estimate of > 1 for the ionisation fraction behind strong shocks but in this case it is fair to assert that the true ionisation fraction is unity and so we simply set it to this value.

To ensure that the energy losses due to the cooling are consistent with the dynamics occurring, we choose our timestep so that the energy lost through radiative energy loss in a cell during any timestep is less than 30% of the total thermal energy of the cell. This is a rather arbitrary figure but we find that it is a suitable cap for damping undesirable side-effects of the dynamics-chemistry operator splitting as will be described in the clipping subsection (§A.6.1). The timestep is also restricted so that no more than 90% of the molecular hydrogen in a cell is dissociated. This, again, is an ad hoc figure but heuristically we would like to give some part of the molecular hydrogen in a post-shock region the chance to survive.

In order to force the numerical scheme to follow the atomic and molecular cooling curves reasonably closely through the timestep we integrate the cooling over the timestep. The criterion for choosing the sub-step values is that the cooling rate coefficients do not change by more than 5% between consecutive sub-steps. We also keep the ionisation of hydrogen to below 10% per sub-step for similar reasons.

As remarked earlier in Sect. 2, we have operator split the dynamics from the chemistry. This is only valid if the Courant number for the dynamical step is quite low. Thus, we require a value of $C \leq 0.6$ although this is largely irrelevant as the restrictions described above present much stronger limitations on the timestep.

A.61. Anomalous cooling

High cooling can often occur at the boundary between a hot, tenuous region and a cool, dense one. This problem was mentioned by Blondin et al. (1990). The difficulty arises from the spatial averaging process that is implicit in all finite differencing schemes. What happens is that the interface between a hot, tenuous region and a cold, dense one is often averaged to slightly hotter, denser values than to which it is entitled. Since radiative cooling goes as ρ^2, this results in a region of anomalously high cooling with a typical width of one cell. In practice for jet simulations where such an interface is common along the edge of the jet beam where it meets the ambient material, this gives rise to a very dense, cold shell around the beam of the jet which

tears through the ambient material in advance of the head of the jet. In order to counter this problem we employ the following technique.

We wish to identify cells which have very high cooling with respect to their neighbours. To do this we define two switches. **SWC** is switched on if

$$\mathcal{L}^{ijk} > \alpha_L \max(\mathcal{L}^{i+1jk}, \mathcal{L}^{i-1jk}) \tag{A.14}$$

and **SWD** is set on if

$$\mathcal{L}^{ijk} > \alpha_L \max(\mathcal{L}^{ij+1k}, \mathcal{L}^{ij-1k}) \tag{A.15}$$

where we have found a value of 5 for α_L to be suitable although as long as it is greater than unity it seems to make little difference up to a couple of orders of magnitude. We then apply the following fix

$$\mathcal{L}^{ijk} = \begin{cases} \mathcal{L}1 & \text{if } \textbf{SWC} \text{ and } \textbf{SWD} \\ \mathcal{L}2 & \text{if } \textbf{SWC} \text{ and not } \textbf{SWD} \\ \mathcal{L}3 & \text{if } \textbf{SWD} \text{ and not } \textbf{SWC} \end{cases} \tag{A.16}$$

where we have defined

$$\mathcal{L}1 = \alpha_L \min\left(\frac{\mathcal{L}^{i+1jk} + \mathcal{L}^{i-1jk}}{2}, \frac{\mathcal{L}^{ij+1k} + \mathcal{L}^{ij-1k}}{2}\right) \tag{A.17}$$

$$\mathcal{L}2 = \alpha_L \frac{\mathcal{L}^{i+1jk} + \mathcal{L}^{i-1jk}}{2} \tag{A.18}$$

$$\mathcal{L}3 = \alpha_L \frac{\mathcal{L}^{ij+1k} + \mathcal{L}^{ij-1k}}{2} \tag{A.19}$$

References

Anders E., Grevesse N., 1989, Geochim. Cosmochim. Acta 53, 197
Balsara D.S., Spicer D.S., 1999, JCP 148, 133
Biro S., Raga A.C., 1994, ApJ 434, 221
Blondin J.M., Fryxell B.A., Königl A., 1990, ApJ 360, 370
Camenzind M., 1998, In: Massaglia S., Bodo G. (eds.), Astrophysical Jets: Open Problems. Gordon and Breach Science Publishers, p. 3
Cerqueira A.H., de Gouveia Dal Pino E.M.D., Herant M., 1997, ApJ 489, L185
Clarke, D.A., Norman, M.L., Burns, J.O., 1986, ApJ 311, L63
Eislöffel J., Mundt R., 1998, AJ 115, 1554
Falle S.A.E.G., Raga A.C., 1995, MNRAS 272, 785
Frank A., Ryu D., Jones T.W., Noriega-Crespo A., 1998, ApJ 494, L79
Gouveia Dal Pino E.M., Benz W., 1994, ApJ 435, 261
Kössl D., Müller E., 1988, A&A 206, 204
Kössl D., Müller E., Hillebrandt W., 1990a, A&A 229, 378
Kössl D., Müller E., Hillebrandt W., 1990b, A&A 229, 397
Laing R.A., 1993, In: Burgarella D., Livio M., O'Dea C.P. (eds.), Astrophysical Jets. Cambridge Univ. Press, p. 95
Lepp S., Shull J.M., 1983, ApJ 270, 578
Lind K.R., Payne D.G., Meier D.L., Blandford R.D., 1989, ApJ 344, 89 (LPMB)
Norman M.L., 1993, In: Burgarella D., Livio M., O'Dea C.P. (eds.), Astrophysical Jets. Cambridge Univ. Press, p. 211
Norman M.L., Smarr L., Winkler K.-H.A., Smith M.D., 1982, A&A 113, 285
Martin P.G., Keogh W.J., 1998, ApJ 499, 793
Micono M., Massaglia S., Bodo G., Rossi P., Ferrari A. 1998, A&A 333, 1001
O'Sullivan S., 1999, PhD Thesis, University of Dublin, Trinity College
O'Sullivan S., 2000, in preparation
Powell K.G., 1994, ICASE Report No. 94-24
Quirk J.J., 1992, ICASE Report No. 92-64
Raga A.C., Canto J., Cabrit S., 1998, A&A 332, 714
Ray T.P., 1996, In: Tsinganos K. (ed.), Solar and Astrophysical MHD Flows. NATO ASI, Heraklion Crete: Kluwer Academic Publishers, p. 539
Ray T.,P., Mundt R., Dyson J.E., Falle S.A.E.G., Raga A.C., 1996, ApJ 468, L103
Ray T.P., Muxlow T.W.B., Axon D.J., Brown A., Corcoran D., Dyson J., Mundt R., 1997, Nat 385, 415
Reipurth B., Hartigan P., Heathcote S., Morse J.A., Bally J., 1997, AJ 114, 757
Smith M.D., 1998, Ap&SS 261, 169
Stone J.M., Hardee P.E., 2000, ApJ in press
Stone J.M., Norman M.L., 1993, ApJ 413, 210
Stone J.M., Norman M.L., 1994, ApJ 420, 237
Strom S.E., Strom K.M., 1987, In: Star Forming Regions. Proceedings of IAU Symposium 115. Tokyo: Reidel Publishing Co., p. 255
Sutherland R.S., Dopita M.A., 1993, ApJS 88, 253
Suttner G., Smith M.D., Yorke H.W., Zinnecker H., 1997, A&A 318, 595
Todo Y., Uchida Y., Sato T., Rosner R., 1993, ApJ 403, 164
Warren-Smith R.F., Scarrott S.M., 1999, MNRAS 305, 875
Wilson M.J., Scheuer P.A.G., 1983, MNRAS 205, 449